Electronic Supplementary Information (ESI)

Manganese oxide-induced strategy to high-performance iron/nitrogen/carbon electrocatalysts with highly exposed active sites

Tao Sun, Qiang Wu, Ou Zhuo, Yufei Jiang, Yongfeng Bu, Lijun Yang, Xizhang Wang, and Zheng Hu**

T. Sun, Prof. Q. Wu, O. Zhuo, Y. F. Jiang, Y. F. Bu, Prof. L. J. Yang, Prof. X. Z. Wang, and Prof. Z. Hu

* Corresponding authors: wqchem@nju.edu.cn (Q. W.); zhenghu@nju.edu.cn (Z. H.)

Content:

ESI-1. Characterization on the hNCNCs support

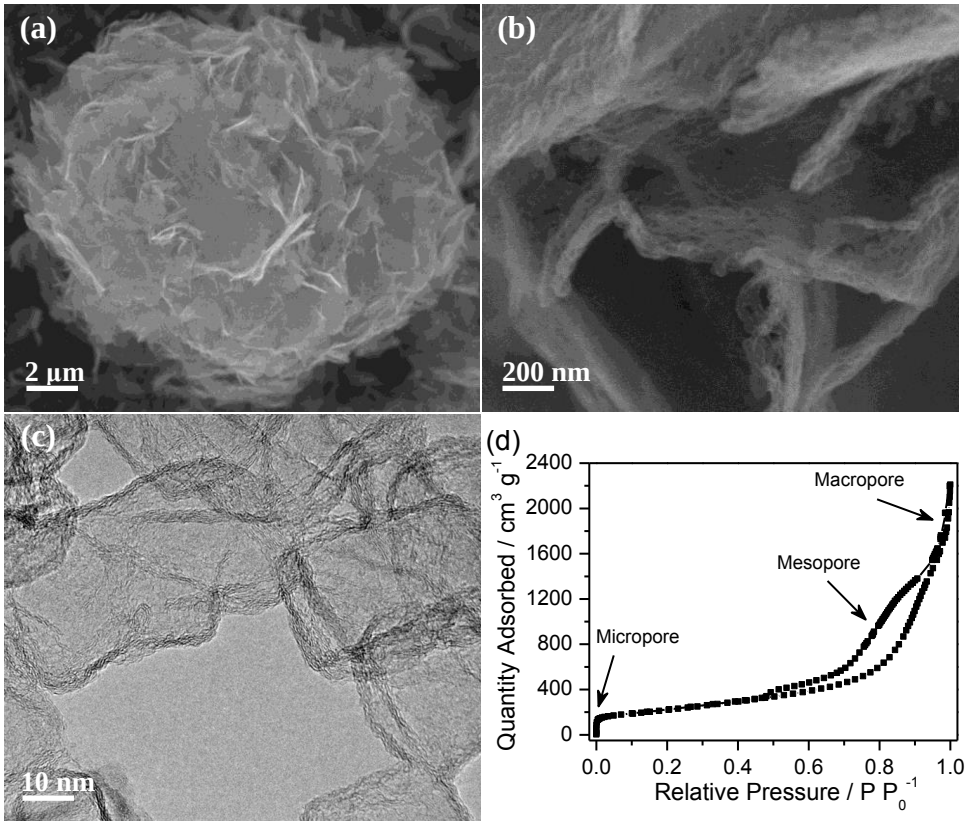

Figure S1. Characterization on the hNCNCs support. (a,b) SEM images; (c) TEM image; (d) N_2 adsorption-desorption isotherm.

The hNCNCs support was prepared at 800 ℃ by *in situ* MgO template method,[1] which is composed of interconnected cuboidal nanocages (30-50 nm) with hierarchical morphology (Figure 1a, Figure S1a-c). N_2 adsorption-desorption isotherm exhibits a typical IV-type curve with two steep uptakes ($P/P_0 < 0.01$, $P/P_0 > 0.97$) and a hysteresis loop ($0.40 < P/P_0 < 0.90$), indicating the coexistence of micropores (< 2 nm), mesopores (2-50 nm) and macropores (> 50 nm). The specific surface area is calculated to be 843 $m^2\ g^{-1}$ using the Brunauer-Emmett-Teller (BET) method based on the adsorption data in Figure S1d.[1] The conductivity is measured to be ~96 S m^{-1} by the method described in our recent paper.[2]

With such a unique morphology and N-participation, as the support, hNCNCs can act as the scaffold to enable the high dispersion of MnO_x nanoparticles onto the surface, leading to the uniform spreading of the PANI layer on hNCNCs (Figure 1).

ESI-2. Uniform dispersion of MnO_x nanoparticles and thereafter PANI on hNCNCs

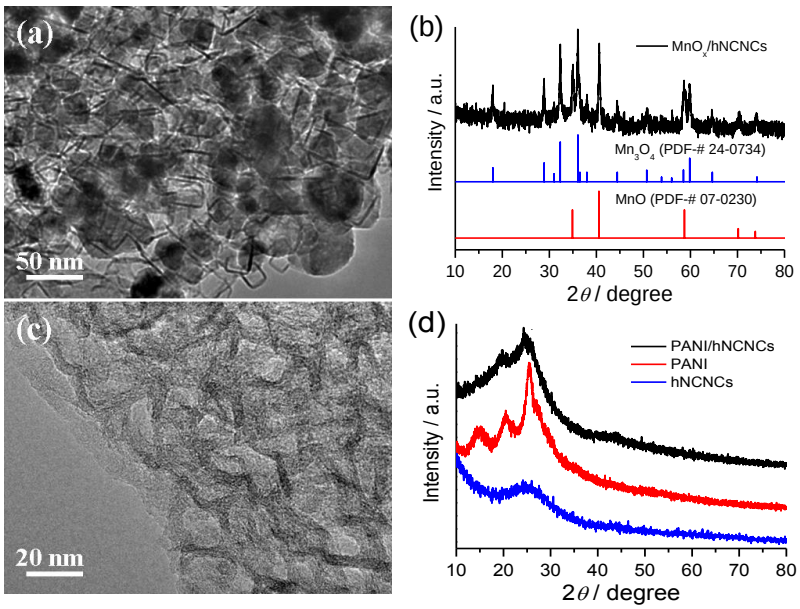

Figure S2. Tracing the intermediates for preparing Fe/N/C. (a,b) TEM image and XRD pattern of the MnO_x/hNCNCs composite; (c,d) TEM image and XRD pattern of the PANI/hNCNCs composite. **Note:** In (d), XRD patterns of hNCNCs and PANI are also presented for reference.[3-6]

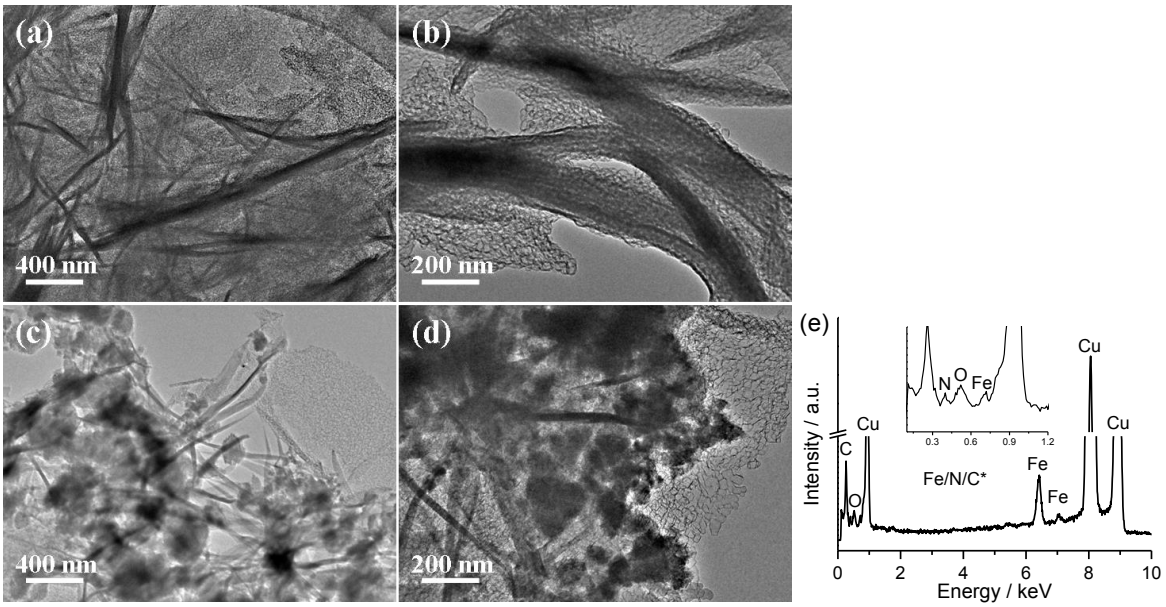

Figure S3. Tracing the intermediates for preparing Fe/N/C*. (a,b) TEM images of the PANI/hNCNCs composite; (c-e) TEM images and EDS spectrum of Fe/N/C*.

In preparing *Fe/N/C by the MnO_x-induced strategy*, MnO_x nanoparticles of 20-60 nm (the mixture of Mn_3O_4 and MnO) are highly dispersed on hNCNCs (Figure 1b, Figure S2a,b). After the reactive-template polymerization, PANI layer uniformly spreads on hNCNCs without self-aggregation, with intimate coupling at the interface (Figure 1c,e, Figure S2c). The following pyrolysis leads to the high dispersion of Fe species for Fe/N/C (Figure 1d,f). No peaks for MnO_x are detected for PANI/hNCNCs, indicating the complete removal of the MnO_x nanoparticles (Figure S2d). By contrast, in preparing *Fe/N/C* by the APS-initiated method*, PANI with irregular morphology non-uniformly spreads on hNCNCs with self-aggregation (Figure S3a,b), quite different from the case in Figure S2c (or Figure 1c,e). The following pyrolysis leads to Fe/N/C* consisting of the multi-shaped carbon species (nanowires, nanoparticles, aggregates, etc.), and the partial encapsulation of Fe species by the PANI-derived carbon (Figure S3c,d), also different from the case of Fe/N/C (Figure 1d,f). Fe, N, C and O signals are detected by EDS (Figure S3e). Such differences in the PANI/hNCNCs intermediates (Figure 1c,e, Figure S2c vs. Figure S3a,b) and final catalysts (Figure 1d,f vs. Figure S3c,d) indicate the advantage of the MnO_x-induced method over the APS-initiated method.

ESI-3. Removal of the extra iron-based particles mixed in Fe/N/C

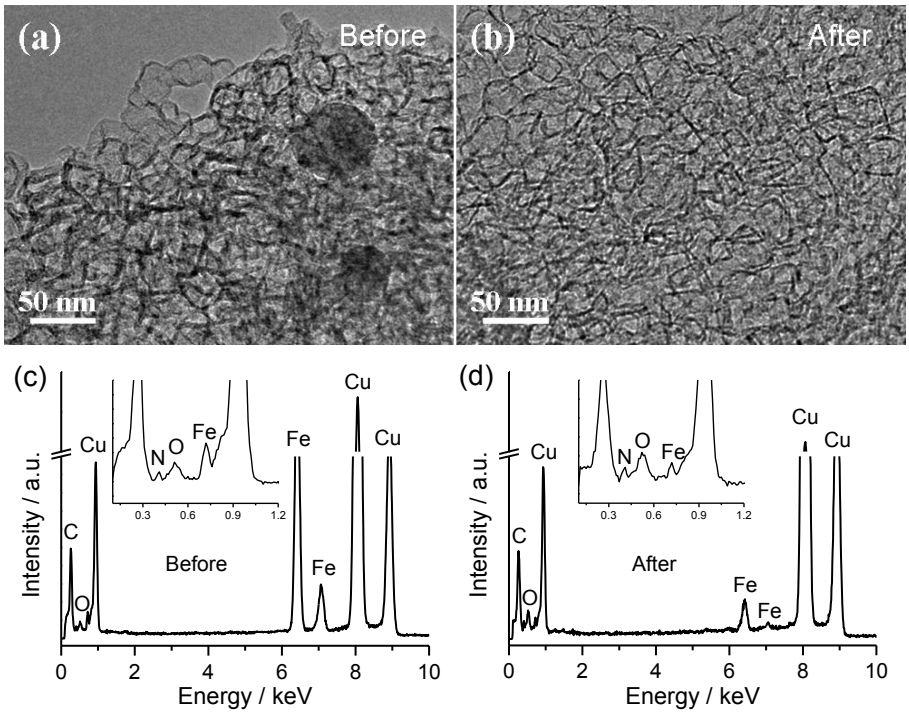

Figure S4. TEM images (a,b) and EDS spectra (c,d) of Fe/N/C catalyst before and after acid leaching.

For Fe/N/C, a few Fe-based particles are observed before acid leaching (Figure S4a), but can be removed by acid leaching (Figure S4b, Figure 1d,f), as supported by EDS analysis (Figure S4c,d). This result indicates these Fe-based particles come from the aggregated iron species without encapsulated. This situation is different from that of the irremovable carbon-encapsulated Fe-based nanoparticles widely observed in literatures as reviewed in the main text. Such difference also means the exposure of Fe-N_x moieties on the surface with the MnO_x-induced strategy, which is beneficial to electrocatalytic reaction.

ESI-4. Raman spectra of Fe/N/C and hNCNCs

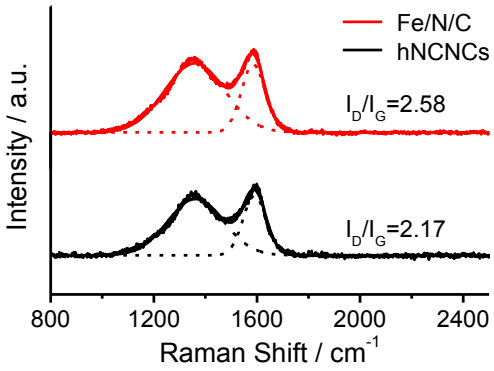

Figure S5. Raman spectra of Fe/N/C and hNCNCs.

Raman spectrum of Fe/N/C has an I_D/I_G value of 2.58, a little larger than the value of 2.17 for hNCNCs. This result suggests that the 'epitaxial' graphitic layers derived from the PANI layer have the lower graphitization degree than hNCNCs, in agreement HRTEM observation (Figure 1f).

ESI-5. Optimization of Fe/N/C-n (n=1,2,3) catalysts and some related characterizations

Table S1. Regulation of the weight ratio of PANI/hNCNCs by changing the loading of MnO_x.

Catalyst	hNCNCs (g)	MnO_x/hNCNCs (g)	PANI/hNCNCs (g)	Weight ratio PANI/hNCNCs
Fe/N/C-1	0.100	0.490	0.135	0.35
Fe/N/C-2	0.100	0.862	0.188	0.88
Fe/N/C-3	0.100	1.020	0.242	1.42

Note: For optimizing Fe/N/C, the corresponding weight ratio of PANI/hNCNCs was tuned in 0.35~1.42.

Table S2. Composition, conductivity and ORR performance of Fe/N/C-n (n=1,2,3) and control catalysts.

Catalyst	XPS [α]				ICP-MS [β]		Conductivity (S m^{-1}) [χ]	ORR performance [δ]	
	Atomic ratio %		Weight ratio %		Weight ratio %			Onset Potential (V vs. RHE)	Current Density (mA cm^{-2} at 0.4 V vs. RHE)
	Fe	N	Fe (C_{Fe})	N	Fe (C_{Fe})	Mn (C_{Mn})			
Fe/N/C-1	0.43	6.07	1.92	6.82	1.95	Undetected	393	0.91	4.625
Fe/N/C-2	0.35	6.37	1.56	7.19	1.57		382	0.92	4.623
Fe/N/C-3	0.48	5.54	2.15	6.24	2.21		341	0.88	3.867
Fe/N/C*	0.44	6.99	1.97	7.85	2.29		267	0.89	3.870
Fe-PANI	0.52	4.46	2.31	4.98	3.31		88	0.82	0.340
Fe-hNCNCs	0.56	6.17	2.50	6.92	2.52		405	0.85	3.946

[α] XPS spectra are shown in Figure S8.

[β] About 10 mg sample was firstly heated in air at 900 ℃ to burn the carbon support. The residual was dissolved in 100 mL HCl (1 mol L^{-1}) and then analyzed by ICP-MS.

[χ] The measurement of conductivity is similar to that described in our recent paper.[2] The pressure used here is 6 MPa.

[δ] Onset potential and current density values are obtained from the RDE curves in Figure 3a. The pyrolysis temperature for preparing the Fe/N/C-2 catalyst is optimized to be 900 °C as learnt from Figure S6 below.

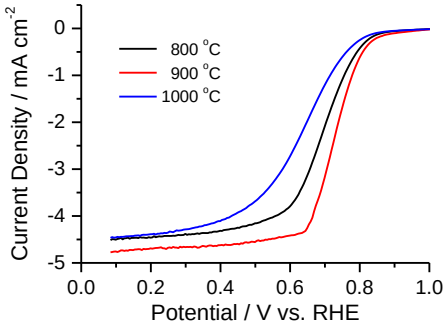

Figure S6. RDE curves (in O_2-saturated 0.5 mol L^{-1} H_2SO_4) of the Fe/N/C-2 catalysts prepared at different pyrolysis temperatures. The optimal one is 900 °C.

Note: For the Fe/N/C-n (n=1,2,3) catalysts, the Fe content measured by ICP-MS well matches with that by XPS, indicating the surficial exposure of all the Fe species. In contrast, for Fe/N/C*, the Fe content by ICP-MS is obviously larger than that by XPS, indicating the partial embedment of the Fe species by the PANI-derived carbon which couldn't be fully detected by XPS. Such a difference comes from the better coupling between PANI and hNCNCs for Fe/N/C than Fe/N/C* before pyrolysis (see ESI-2), as expected (Scheme 1).

The Fe/N/C-n (n=1,2,3) catalysts have better conductivities than Fe/N/C*, which could also be assigned to the excellent coupling between the PANI-derived carbon and hNCNCs for the former.

Fe/N/C-2 pyrolyzed at 900 °C is the optimized catalyst, which is renamed as Fe/N/C and fully studied.

Table S3. Specific surface areas and pore volumes of Fe/N/C, Fe/N/C*, Fe-hNCNCs and Fe-PANI.

Catalyst	Fe/N/C	Fe/N/C*	Fe-hNCNCs	Fe-PANI
Specific Surface Areas (m^2 g^{-1})	598	626	772	389
Pore Volume (cm^3 g^{-1})	2.91	2.40	2.62	0.56

Note: Without using the support, Fe-PANI possesses the lowest specific surface area (From Figure S7).

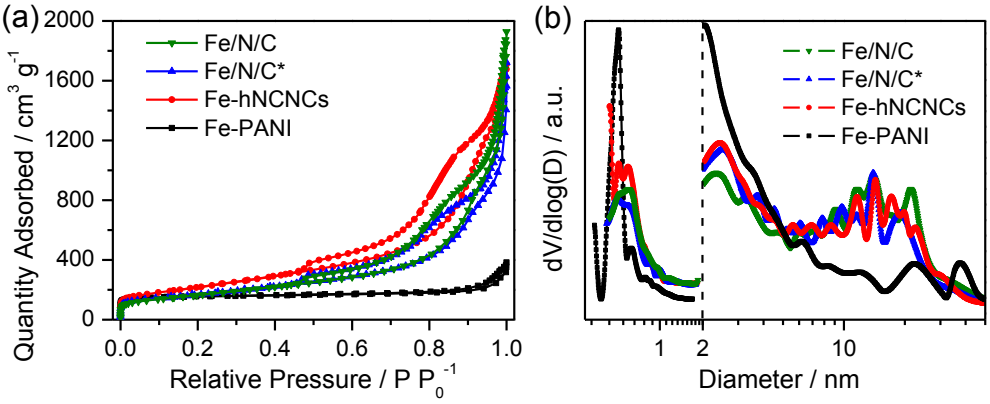

Figure S7. N_2 adsorption-desorption isotherms (a) and pore size distributions (b) of Fe/N/C, Fe/N/C*, Fe-hNCNCs and Fe-PANI.

ESI-6. XPS spectra of Fe/N/C-n (n=1,2,3) and control catalysts

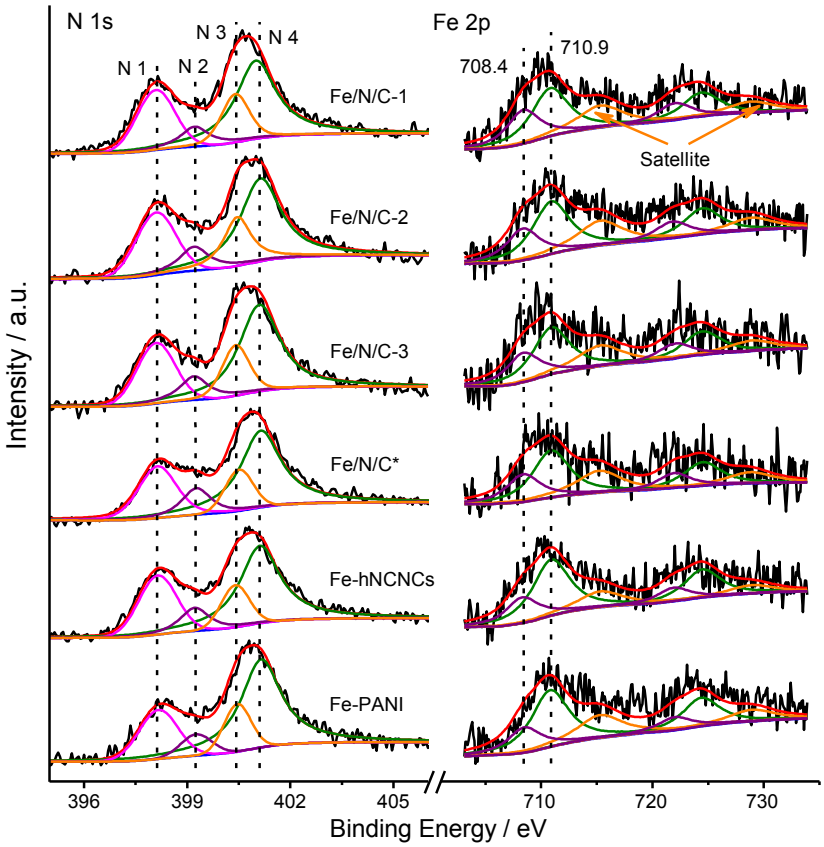

Figure S8. XPS spectra of the Fe/N/C-n (n=1, 2, 3) and control catalysts. For N 1s: N1 (pyridinic N)_398.20 ± 0.10 eV, N2 (Fe-N_x)_399.25 ± 0.05 eV, N3 (pyrrolic N)_400.45 ± 0.05 eV, N4 (graphitic N)_401.10 ± 0.10 eV. For Fe 2p: $2p_{3/2}$ of Fe(III)_710.80-710.90 eV, $2p_{3/2}$ of Fe(II)_708.30-708.50 eV, Satellite_715.30-715.60 eV.

ESI-7. Elemental mapping and XRD characterizations of Fe/N/C

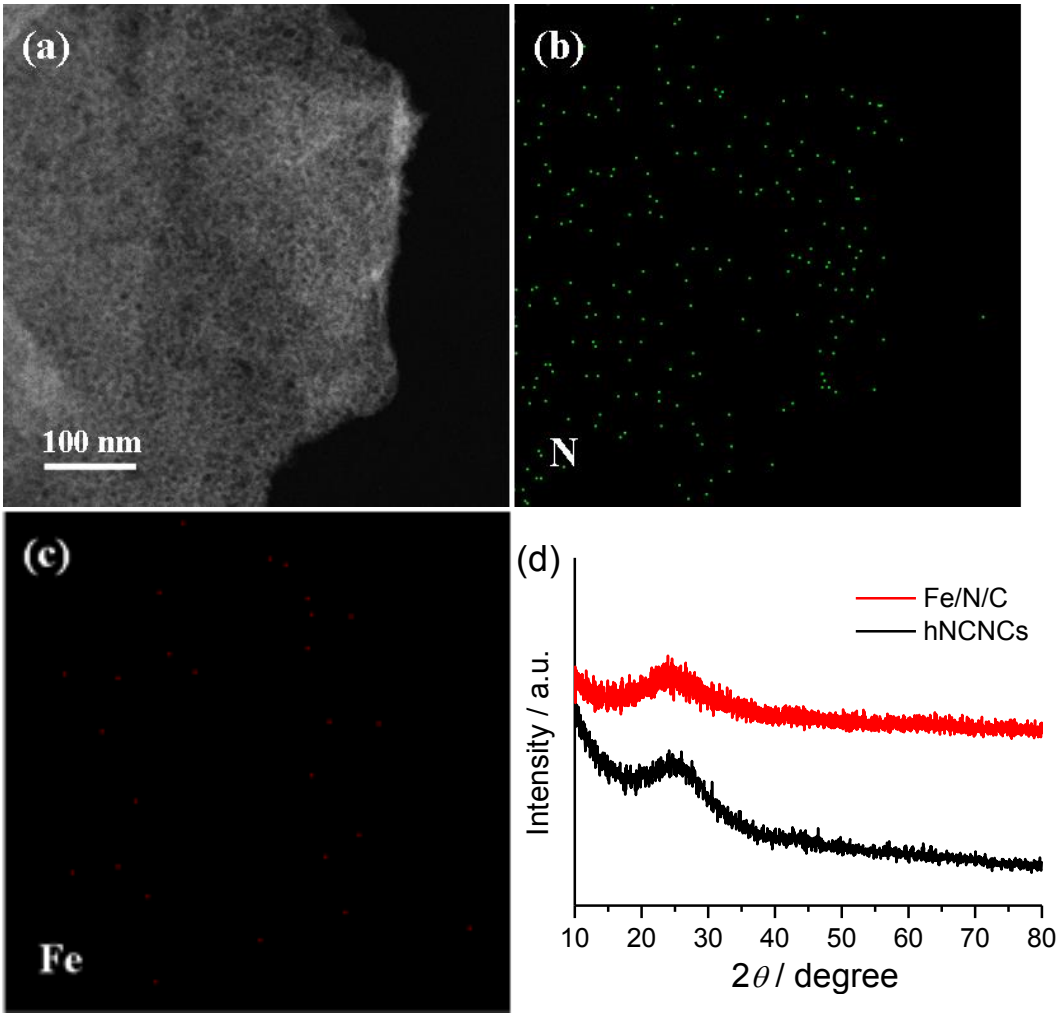

Figure S9. Characterizations of Fe/N/C. (a) TEM image; (b) N mapping; (c) Fe mapping; (d) XRD pattern. In (d), the corresponding XRD pattern of hNCNCs is also provided for comparison. **Note:** XRD data with Co target are converted into the ones with Cu target for convenient reference to the PDF cards.

The elemental mappings of N and Fe indicate the high dispersion of N and Fe species (Figure S9a-c). XRD pattern doesn't show any diffraction peaks for Fe species, only with the peak for (002) plane of carbon, in agreement with the high dispersion of Fe (Figure S9c, d).

ESI-8. RDE and CV tests of the Fe/N/C-n (n=1,2,3) catalysts

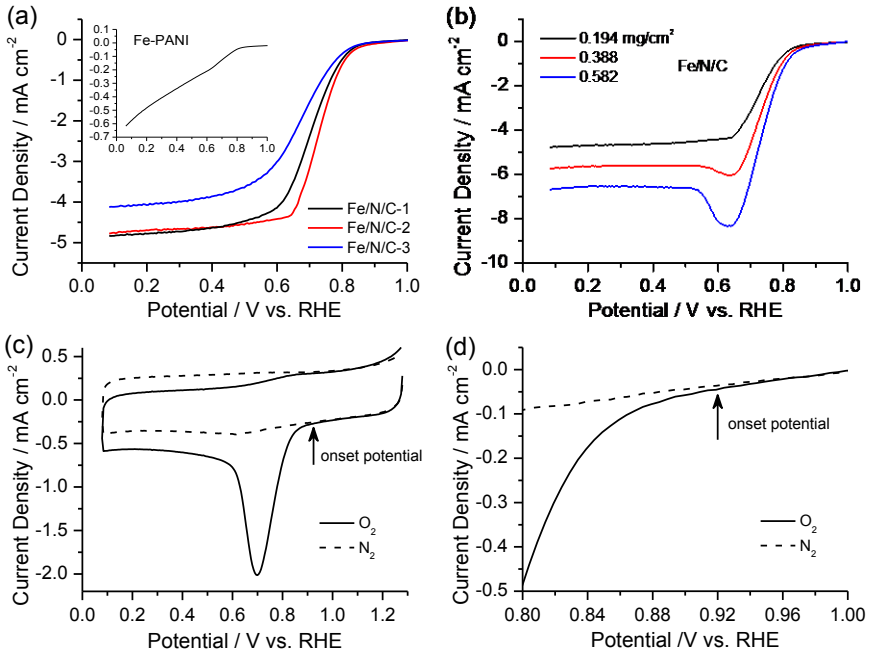

Figure S10. RDE and CV tests of the Fe/N/C-n (n=1,2,3) in O_2- or N_2-saturated 0.5 mol L^{-1} H_2SO_4 solution. (a) RDE curves (O_2-saturated). Inset: Fe-PANI for reference with an E_{on} of ~0.82 V (vs. RHE) and the low current density. Fe/N/C-2 is the optimized catalyst, renamed as Fe/N/C in the main text; (b) RDE curves (O_2-saturated) of Fe/N/C with different loadings on electrode; (c,d) CV and RDE curves of Fe/N/C (O_2- and N_2-saturated), respectively. Onset potential (E_{on}) is defined as the separating point of CV or RDE as arrowed at 0.92 V.

ESI-9. Test of electron transfer number of Fe/N/C

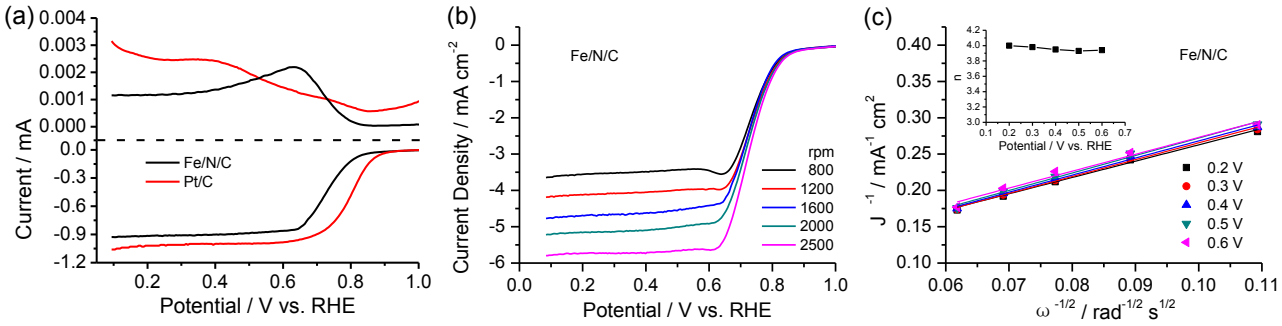

Figure S11. Test of electron transfer number (*n*) of Fe/N/C. (a) RRDE curve of Fe/N/C with Pt/C as a reference; (b) RDE curves at different rotation rates (800-2500 rpm); (c) Koutecky-Levich plot. Inset: *n* value vs. potential.

Note:

RRDE test in Figure S11a gives the electron transfer number (*n*) of Fe/N/C as shown in Figure 3b.

In addition, we have also estimated the *n* value using Koutecky-Levich method according to the RDE curves at different rotation rates (Figure S11b,c).[7,8]

The *n* values obtained by the two different methods are highly consistent with each other.

ESI-10. Stability of Fe/N/C

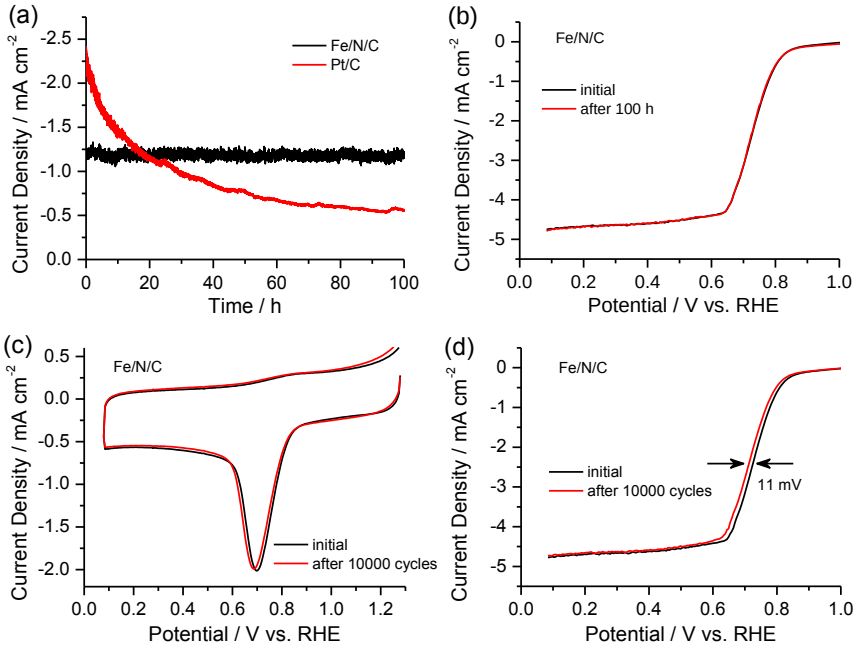

Figure S12. Stability of Fe/N/C. (a) Original CP curves corresponding to Figure 3c; (b) RDE curves before and after 100 h test; (c,d) CV and RDE curves of Fe/N/C before and after 10000 cycles. **Note:** In (c) and (d), the accelerated durability tests were carried out with scan rate of 100 mV s^{-1} between -0.2 and 1.0 V (vs. Ag/AgCl) under magnetic stirring and oxygen bubbling of 15 sccm.

ESI-11. ORR activities of typical M/N/C (M = Fe or Co) catalysts in acidic medium

Table S4. ORR activities of typical M/N/C (M = Fe or Co) catalysts in acidic medium.

Acidic Medium	Catalyst Amount (mg cm^{-2})	Scan Rate (mV s^{-1})	Rotation Rate (rpm)	Onset Potential (V vs. RHE)	Current Density (mA cm^{-2}) (at 0.4 V vs. RHE)	Fe-based Particles Presence	Reference
0.5 M H_2SO_4	0.600	10	900	0.93	3.865	Yes	[10]
0.5 M H_2SO_4	0.600	10	1600	0.92	4.326	-	[11]
0.1 M H_2SO_4	0.600	10	900	0.92	3.975	-	[9]
0.1 M $HClO_4$	0.400	10	1600	0.93	5.057	-	[12]
0.1 M $HClO_4$	0.400	10	1600	0.91	5.064	-	[13]
0.1 M $HClO_4$	0.400	10	1600	0.92	4.875	Yes	[14]
0.1 M $HClO_4$	0.815	10	1600	0.91	4.814	-	[15]
0.1 M $HClO_4$	0.600	10	1600	0.91	5.029	-	[16]
0.5 M H_2SO_4	0.400	10	1600	0.88	3.503	Yes	[17]
0.1 M $HClO_4$	0.600	10	1600	0.88	5.531	-	[18]
0.5 M H_2SO_4	0.600	10	1600	0.89	4.232	Yes	[19]
0.1 M $HClO_4$	0.600	10	1600	0.88	5.326	-	[20]
0.5 M H_2SO_4	0.245	10	1600	0.87	3.961	Yes	[21]
0.1 M $HClO_4$	0.510	10	1600	0.86	4.904	Yes	[22]
0.5 M H_2SO_4	0.800	10	1500	0.85	3.958	-	[23]
0.5 M H_2SO_4	1.000	10	1600	0.86	3.318	-	[24]
0.5 M H_2SO_4	0.400	10	1600	0.83	3.812	Yes	[25]
0.5 M H_2SO_4	0.200	10	1600	0.81	4.271	-	[26]
0.5 M H_2SO_4	0.500	10	1600	0.80	2.949	-	[27]
0.5 M $HClO_4$	0.255	10	1600	0.80	3.033	Yes	[28]
0.5 M H_2SO_4	0.194	10	1600	0.92	4.623	No	
0.5 M H_2SO_4	0.388	10	1600	0.92	5.624	No	This study
0.5 M H_2SO_4	0.582	10	1600	0.92	6.588	No	

"-": TEM image of the catalyst is not available in the paper.

The Fe/N/C catalyst prepared by MnO_x-induced strategy in this study presents the top-ranking level of the onset potential and the highest current density to date.

ESI-12. Parameter A of different Fe/N/C catalysts at different potentials (V vs. RHE)

Table S5. Parameter *A* of different Fe/N/C catalysts at different potentials (V vs. RHE).

Catalyst	Fe (wt.%)	0.2	0.3	0.4	0.5	0.6	0.7	0.75	0.8	Reference
PANI-Fe/Silica colloid	6.52	0.067	0.067	0.066	0.064	0.062	0.049	0.024	0.005	[11]
PANI-Fe/C	4.35	0.114	0.110	0.080	0.064	0.038	0.013	0.004	0.001	[11]
PFeTTPP- 700	4.12	0.171	0.171	0.168	0.165	0.156	0.108	0.059	0.017	[12]
PFeTTPP- 1000	4.95	0.151	0.150	0.148	0.146	0.141	0.118	0.073	0.018	[12]
$Zn(eIm)_2TPIP$-Fe	1.14	0.661	0.650	0.642	0.635	0.620	0.576	0.449	0.189	[13]
$Zn(4abIm)_2TPIP$-Fe	0.79	0.928	0.920	0.898	0.882	0.853	0.746	0.530	0.211	[13]
FeIM/ZIF-8	5.29	0.136	0.135	0.133	0.131	0.126	0.106	0.072	0.026	[14]
Fe-N-rGO	1.73	0.317	0.307	0.292	0.256	0.186	0.084	0.042	0.015	[17]
Fe-N-GC-900	0.95	0.564	0.562	0.560	0.553	0.537	0.419	0.214	0.062	[18]
Fe-C-PANI/NSA	3.00	0.194	0.190	0.186	0.179	0.167	0.121	0.060	0.014	[22]
Fe–N-MWCNT	1.89	0.321	0.307	0.292	0.266	0.216	0.118	0.058	0.014	[25]
Fe-N_x/rGO	3.08	0.125	0.120	0.111	0.086	0.042	0.011	0.005	0.003	[27]
UK63-Fe	1.63	0.476	0.467	0.464	0.460	0.465	0.457	0.459	0.256	[29]
Fe1/50/50-NC_{Z8}-700(5)-950	2.40	0.145	0.141	0.136	0.130	0.120	0.101	0.080	0.040	[30]
Fe1/50/50-NC_{Z8FA}-1050(5)	1.80	0.184	0.179	0.174	0.164	0.139	0.079	0.038	0.015	[30]
Fe1/20/80-Z8-1050	3.30	0.098	0.098	0.095	0.090	0.076	0.042	0.021	0.009	[30]
Fe-hNCNCs	2.52	0.518	0.499	0.468	0.413	0.294	0.123	0.063	0.026	
Fe/N/C*	2.29	0.526	0.517	0.504	0.485	0.441	0.241	0.122	0.046	
Fe/N/C-1	1.95	0.731	0.723	0.708	0.684	0.635	0.367	0.195	0.076	This study
Fe/N/C-2	**1.57**	**0.892**	**0.887**	**0.879**	**0.867**	**0.840**	**0.606**	**0.325**	**0.120**	
Fe/N/C-3	2.21	0.550	0.537	0.521	0.492	0.406	0.210	0.114	0.048	

Table S5 summarizes the *A* values of the state-of-the-art M/N/C catalysts in acidic medium. It can be observed that the *A* value of the Fe/N/C catalyst locates at the top ranking level in M/N/C catalysts.

ESI-13. Qualitative estimation on the exposed active sites with SCN^- probe ions

As revealed by Sun et al.,[9] SCN^- ions can cover Fe-N_x moieties for their high affinity to Fe species. Thus, by adding SCN^- ions into the O_2-saturated H_2SO_4 solution, ORR activity of the Fe-based catalyst will remarkably decrease. The more exposed active sites the catalyst has, the greater the ORR activity decreases. With this approach, we examined the relative amount of exposed Fe-N_x active sites for Fe/N/C, Fe/N/C* and Fe-hNCNCs. The residual ORR activity below the 0.7 V (vs. RHE) comes from the Fe^{2+} species since SCN^- ions only affects the Fe^{3+}, as described in the literature.[9]

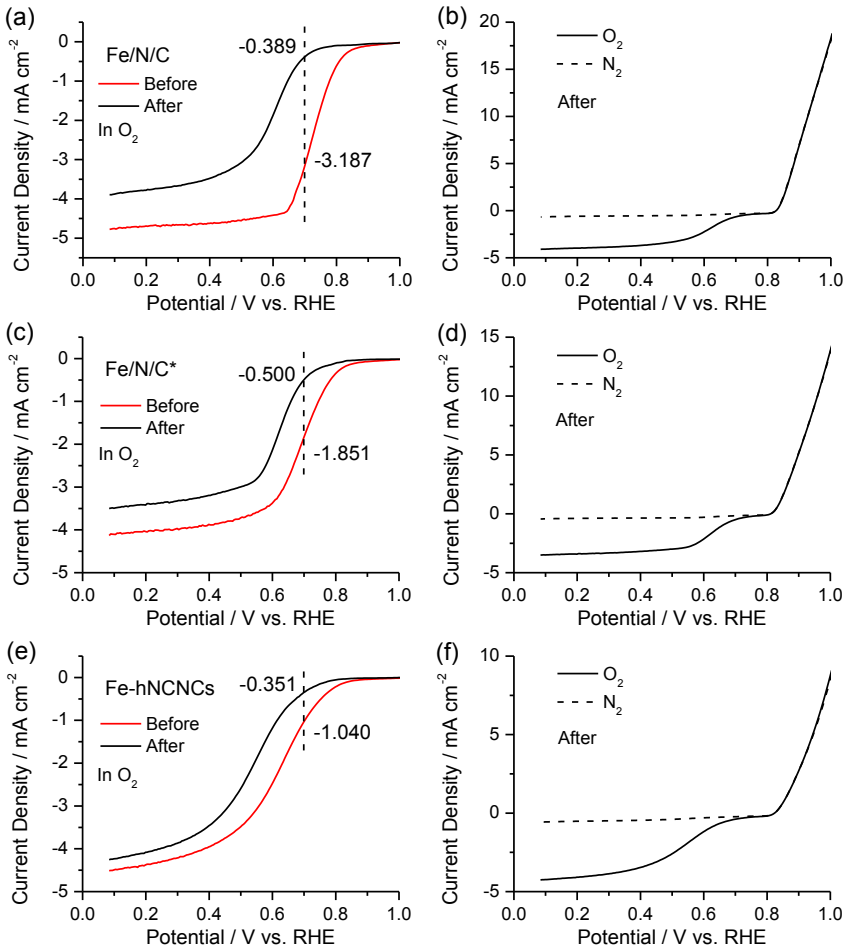

Figure S13. RDE curves of the catalysts. (a,c,e) before and after adding SCN^- ions into the O_2-saturated H_2SO_4 solution. (b,d,f) after adding SCN^- ions into the O_2- and N_2-saturated H_2SO_4 solution. (a,b) Fe/N/C; (c,d) Fe/N/C*; (e,f) Fe-hNCNCs. The SCN^- ion concentration is 5 mmol L^{-1}.

In Figure S13b,d,f, the rapid increase of current density at potential > 0.81 V arises from the reduction of the SCN^- ions rather than ORR,[9] which is highly overlapped in O_2- or N_2-saturated solution. Hence, by subtracting this contribution, the RDE curves after adding the SCN^- in O_2-saturated case can be obtained as presented in Figure S13a,c,e (in black) for comparison.

Table S6. Current density of Fe/N/C, Fe/N/C* and Fe-hNCNCs at 0.7 V before and after adding SCN^- ions.

Catalyst	Current Density (mA cm^{-2}) Before	Current Density (mA cm^{-2}) After	Decrease (mA cm^{-2})
Fe/N/C	-3.187	-0.389	**2.798**
Fe/N/C*	-1.851	-0.500	1.351
Fe-hNCNCs	-1.040	-0.351	0.689

Note: Fe/N/C presents the largest decrease of the current density (2.798 mA cm^{-2}), indicating the most exposed active sites.

ESI-14. Fe/N/C$^{\#}$ prepared by the MnO_x-induced strategy with the hCNCs support

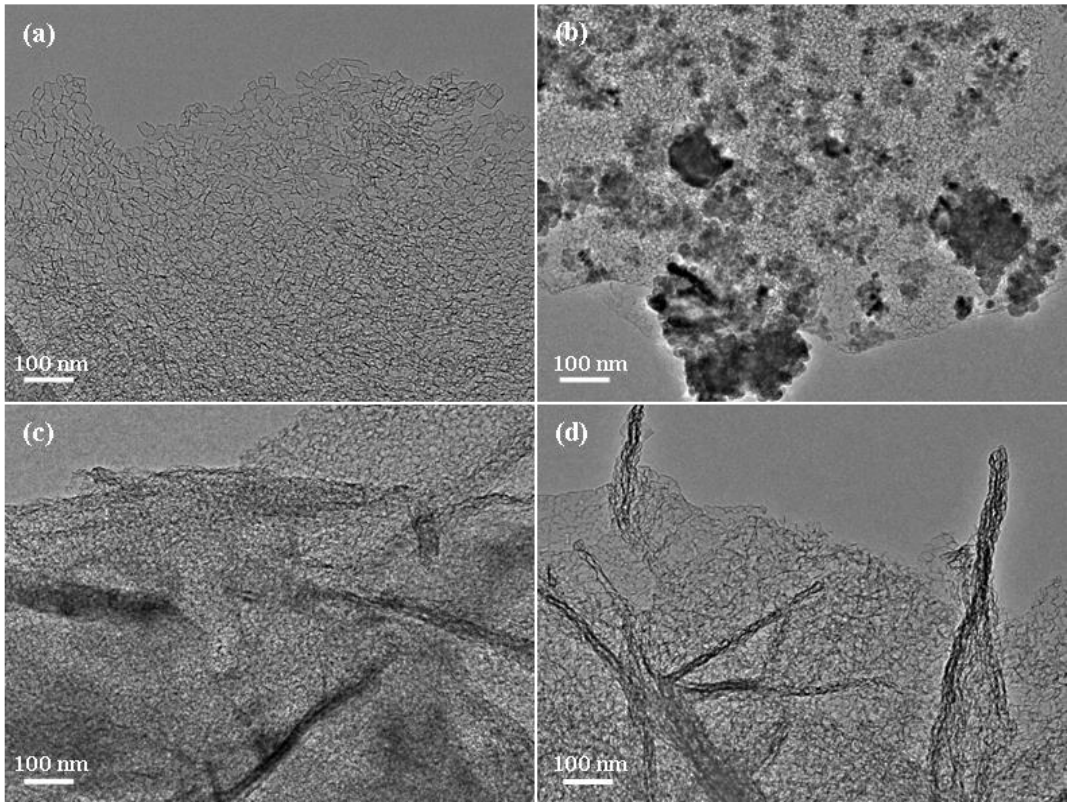

Figure S14. TEM characterizations on the evolution of the products in preparing Fe/N/C$^{\#}$. (a) hCNCs; (b) MnO_x/hCNCs; (c) PANI/hCNCs; (d) Fe/N/C$^{\#}$.

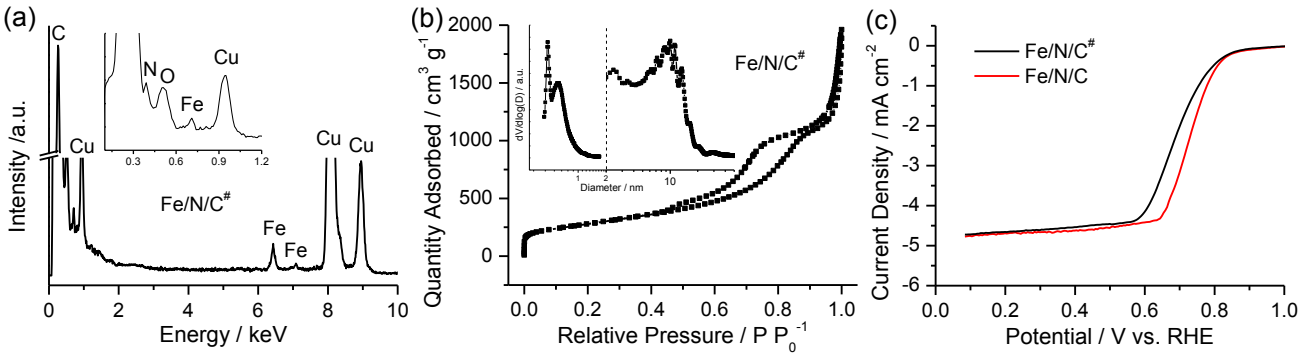

Figure S15. Characterizations on Fe/N/C$^{\#}$. (a) EDS spectrum; (b) N_2 adsorption-desorption isotherm and pore size distribution; (c) RDE curve in O_2-saturated 0.5 mol L^{-1} H_2SO_4 solution. RDE curve of Fe/N/C is also presented in (c) for comparison.

In comparison with the case for preparing Fe/N/C (Figure 1), the distribution of MnO_x nanoparticles on the hCNCs is not so uniform as that on hNCNCs (Figure S14b vs. Figure 1b). Consequently, the coupling of the PANI, thereof the PANI-derived carbon, with hCNCs is not as good as that with hNCNCs (Figure S14c vs. Figure 1c; Figure S14d vs. Figure 1d). These results indicate the role of nitrogen in the hNCNCs support.

In comparison with Fe/N/C, Fe/N/C$^{\#}$ has the similar composition (Figure S15a vs. Figure 2a), specific surface area (647 m^2 g^{-1}) and pore volume (2.66 cm^3 g^{-1}) (Figure S15b vs. Figure S7). But the ORR performance of Fe/N/C$^{\#}$ is a little inferior to that of Fe/N/C (Figure S15c), also reflecting the role of N in the hNCNCs support.

ESI-15. Characterizations of the control catalysts

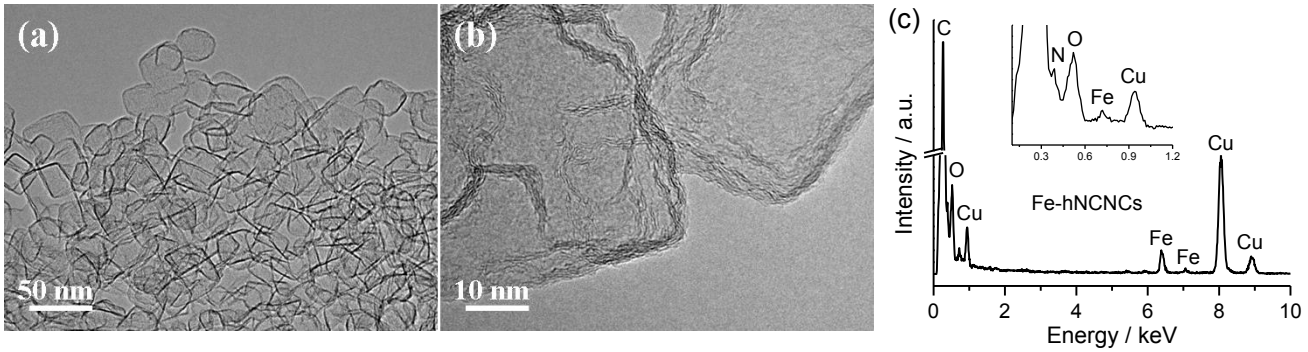

Figure S16. TEM images and EDS spectrum of Fe-hNCNCs.

Fe-hNCNCs presents the morphology of the nanocage without observable Fe-based nanoparticles (Figure S16a,b). Fe, N, C and O signals are detected by EDS (Figure S16c).

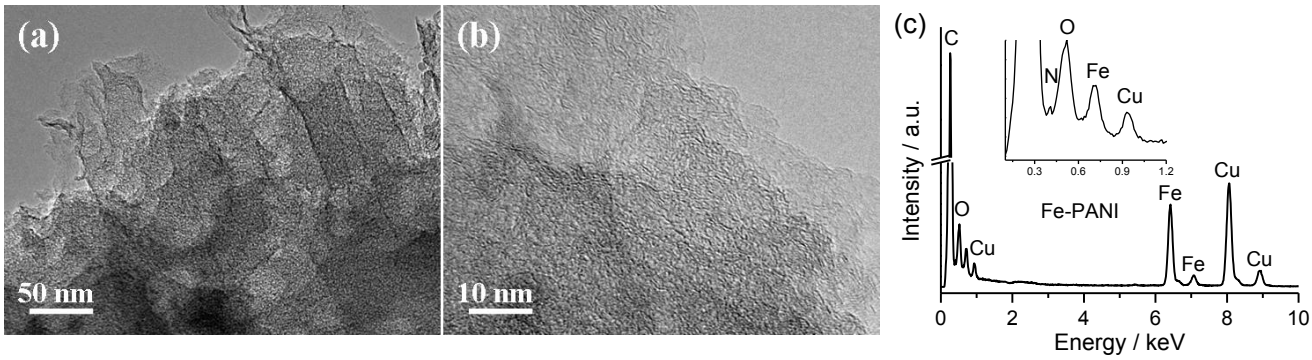

Figure S17. TEM images and EDS spectrum of Fe-PANI.

Fe-PANI presents irregular carbon layers graphitized to certain degree (Figure S17a,b). Fe, N, C and O signals are detected by EDS (Figure S17c).

References:

[1] J. Zhao, H. W. Lai, Z. Y. Lyu, Y. F. Jiang, K. Xie, X. Z. Wang, Q. Wu, L. J. Yang, Z. Jin, Y. W. Ma, J. Liu, Z. Hu, *Adv. Mater*. **2015**, *27*, 3541-3545.

[2] Z. Y. Lyu, D. Xu, L. J. Yang, R. C. Che, R. Feng, J. Zhao, Y. Li, Q. Wu, X. Z. Wang, Z. Hu, *Nano Energy* **2015**, *12*, 657-665.

[3] W. Chen, R. B. Rakhi, H. N. Alshareef, *J. Phys. Chem. C* **2013**, *117*, 15009-15019.

[4] W. Qiu, L. Ma, M. Y. Gan, Y. Q. Bai, D. D. Fu, Z. T. Li, F. F. Chen, *Ploym. Eng. Sci*. **2014**, *53*, 1631-1636.

[5] Z. M. Zhang, M. X. Wan, Y. Wei, *Adv. Funct. Mater*. **2006**, *16*, 1100-1104.

[6] J. Yan, Y. W. Yang, L. Ma, M. Y. Gan, X. Li, *Ploym. Composite* **2015**, *36*, 1541-1545.

[7] D. S.Yu, Q. Zhang, L. M. Dai, *J. Am. Chem. Soc*. **2010**, *132*, 15127-15129.

[8] G. Yang, W. Choi, X. Pu, C. Yu, *Energy Environ. Sci*. **2015**, *8*, 1799-1807.

[9] Q. Wang, Z. Y. Zhou, Y. J. Lai, Y. You, J. G. Liu, X. L. Wu, E. Terefe, C. Chen, L. Song, M. Rauf, N. Tian, S. G. Sun, *J. Am. Chem. Soc.* **2014**, *136*, 10882-10885.

[10] G. Wu, K. L. More, C. M. Johnston, P. Zelenay, *Science* **2011**, *332*, 443-447.

[11] H. W. Liang, W. Wei, Z. S. Wu, X. L. Feng, K. Müllen, *J. Am. Chem. Soc*. **2013**, *135*, 16002-16005.

[12] S. W. Yuan, J. L. Shui, L. Grabstanowicz, C. Chen, S. Commet, B. Reprogle, T. Xu, L. P. Yu, D. J. Liu, *Angew. Chem. Int. Ed*. **2013**, *52*, 8349-8353.

[13] D. Zhao, J. L. Shui, L. R. Grabstanowicz, C. Chen, S. M. Commet, T. Xu, J. Lu, D. J. Liu, *Adv. Mater*. **2014**, *26*, 1093-1097.

[14] D. Zhao, J. L. Shui, C. Chen, X. Q. Chen, B. M. Reprogle, D. P. Wang, D. J. Liu, *Chem. Sci*. **2012**, *3*, 3200-3205.
[15] H. C. Huang, C. H. Wang, I. Shown, S. T. Chang, H. C. Hsu, H. Y. Du, L. C. Chen, K. H. Chen, *J. Mater. Chem. A* **2013**, *1*, 14692 -14699.
[16] W. Ding, L. Li, K. Xiong, Y. Wang, W. Li, Y. Nie, S. G. Chen, X. Q. Qi, Z. D. Wei, *J. Am. Chem. Soc*. **2015**, *137*, 5414-5420.
[17] H. R. Byon, J. Suntivich, Y. S. Horn, *Chem. Mater*. **2011**, *23*, 3421-3428.
[18] A. Kong, X. F. Zhu, Z. Han, Y. Y. Yu, Y. B. Zhang, B. Dong, Y. K. Shan, *ACS Catal*. **2014**, *4*, 1793-1800.
[19] M. Ferrandon, A. J. Kropf, D. J. Myers, K. Artyushkova, U. Kramm, P. Bogdanoff, G. Wu, C. M. Johnston, P. Zelenay, *J. Phys. Chem. C* **2012**, *116*, 16001-16013.
[20] Y. Wang, A. G. Kong, X. T. Chen, Q. P. Lin, P. Y. Feng, *ACS Catal*. **2015**, *5*, 3887-3893.
[21] L. B. Lv, T. N. Ye, L. H. Gong, K. X. Wang, J. Su, X. H. Li, J. S. Chen, *Chem. Mater*. **2015**, *27*, 544-549.
[22] R. P. Zheng, Z. Y. Mo, S. J. Liao, H. Y. Song, Z. Y. Fu, P. Y. Huang, *Carbon* **2014**, *69*, 132-141.
[23] K. Kamiya, K. Hashimoto, S. J. Nakanishi, *Chem. Commun*. **2012**, *48*, 10213-10215.
[24] R. Z. Jiang, D. Chu, *J. Power Sources* **2014**, *245*, 352-361.
[25] H. R. Byon, J. Suntivich, E. J. Crumlin, Y. S. Horn, *Phys. Chem. Chem. Phys*. **2011**, *13*, 21437-21445.
[26] S. Li, D. Q. Wu, H. W. Liang, J. Z. Wang, X. D. Zhuang, Y. Y. Mai, Y. Z. Su, X. L. Feng, *ChemSusChem* **2014**, *7*, 3002-3006.
[27] A. H. A. M. Videla, S. Ban, S. Specchia, L. Zhang, J. J. Zhang, *Carbon* **2014**, *76*, 386-400.
[28] T. Palaniselvam, B. P. Biswal, R. Banerjee, S. Kurungot, *Chem. Eur. J*. **2013**, *19*, 9335-9342.
[29] F. Jaouen, J. Herranz, M. Lefèvre, J. Dodelet, U. I. Kramm, I. Herrmann, P. Bogdanoff, J. Maruyama, T. Nagaoka, A. Garsuch, J. R. Dahn, T. Olson, S. Pylypenko, P. Atanassov, E. A. Ustinov, *ACS Appl. Mater. Interfaces* **2009**, *1*, 1623-1639.
[30] A. Morozan, M. T. Sougrati, V. Goellner, D. Jones, L. Stievano, F. Jaouen, *Electrochim. Acta* **2014**, *119*, 192-205.